Geophysical Research Letters

Supporting Information for

Global Frictional Equilibrium via Stochastic, Local Coulomb Frictional Slips

Shihuai Zhang and Xiaodong Ma

Department of Earth Sciences, ETH Zürich, Zürich, Switzerland

Contents of this file

Introduction

In this supplementary material, we expand on the methods and results to complement the main manuscript. In Text S1, we describe how to calculate the shear and normal stresses on fractures and discuss the major assumptions adopted in this model. In Text S2, we elaborate on the slip cascades and their contribution to the global stress/strain fields, followed by an example displaying the iterative process in the context of normal faulting stress regime. We then show the stress evolution in the deterministic case where all fractures have the same frictional coefficient in Text S3. Monte Carlo simulation and system uncertainty analysis are detailed in Text S4. For each frictional coefficient distribution, finally in Text S5, simulation results in the context of reverse faulting regime are provided for comparison.

Text S1. Individual Fractures, Local Frictional Slips

Given a stress tensor $\boldsymbol{\sigma}$ applied remotely at the model boundary, the stress acting on any arbitrarily-oriented fictitious fracture plane can be resolved by transformation. The normal and shear stress component (σ_{n} and τ) on a fracture plane can be resolved with the plane's unit normal and shear vector (**n** and **s**) (Davy et al., 2018):

$$\sigma_{\mathrm{n}} = \mathbf{n} \cdot \boldsymbol{\sigma} \cdot \mathbf{n} \tag{S1}$$

$$\tau = \mathbf{n}^{\mathrm{T}} \cdot \boldsymbol{\sigma} \cdot \mathbf{s} \tag{S2}$$

where

$$\mathbf{s} = \frac{\mathbf{s}_g}{|\mathbf{s}_g|},\ \mathbf{s}_g^{\mathrm{T}} = \mathbf{n}^{\mathrm{T}} \cdot \boldsymbol{\sigma} \cdot \left(\mathbf{I} - \mathbf{n} \otimes \mathbf{n}^{\mathrm{T}}\right) \tag{S3}$$

where **I** is the identity matrix. Intuitively, the Mohr diagram graphically represents the initial stresses acting on fractures, as shown in Figure 2. In our model, the fracture orientation is differentiated by the angle (θ) between the normal to the fracture and the positive hortizontal axis of the model's global coordinates (Figure S1). Note that, for convenience, we only consider the normal vector of the upward facing fracture side, i.e., $\theta \in [0,180°]$.

Local stress fluctuations induced by nearby fracture interactions can be profound in a rock mass. However, such effect is not considered in this model. By assuming a uniform spatial distribution of fracture centers, i.e., no fracture clusters exist, strong fracture interactions can be plausibly circumvented. The mutually opposite effects of stress shielding and amplification near fractures tend to balance out globally, given the statistical significance of assuming uniform fracture orientations (Kachanov, 1992). Such assumptions have been validated by comparing the theoretically predicted results either with numerical simulations (Grechka and Kachanov, 2006) or with laboratory observations (Katz and Reches, 2004), and have been widely adopted to quantify the effective properties of fractured rock masses (e.g., Healy, 2008; Davy et al., 2018).

Text S2. More on Upscaling Slip Cascades and Iterative Time Steps

Slip rate within a time step

The slip rate is considered variable, which is dependent on the past slip history and stress state (Dieterich, 1979; Ruina, 1980, Sleep, 2006). To reflect this in the iterations, a simple linear relationship between fracture slip rate and shear stress difference $\Delta\tau$ is proposed:

$$\frac{d\bar{\mathbf{d}}_{\mathrm{s}}}{dt} = (\eta\Delta\tau)\mathbf{s} \tag{S4a}$$

$$\frac{d\bar{\mathbf{d}}_{\mathrm{n}}}{dt} = (\beta\cdot\eta\Delta\tau)\mathbf{n} \tag{S4b}$$

where η is defined as slip rate parameter with the dimension of length/(stress·time), similar to the fluidity parameter of classical viscoplasticity theory (Perzyna, 1966; Napier and Malan, 1997).

In discrete form, the relative shear and normal displacement increments can be further expressed as:

$$\Delta\left|\bar{\mathbf{d}}_{\mathrm{s}}\right|_j = \left(\eta_j\Delta\tau_{j-1}\right)\cdot\Delta t \tag{S5a}$$

$$\Delta\left|\bar{\mathbf{d}}_{\mathrm{n}}\right|_j = \left(\beta\cdot\eta_j\Delta\tau_{j-1}\right)\cdot\Delta t \tag{S5b}$$

where

$$\Delta t = t_j - t_{j-1}, j = 1,2,3,\ldots \tag{S5c}$$

which implies that the updated results at the end of the previous time step (j-1) serve as the new input and are kept constant over the current time step (j). If frictional slip is assumed to occur completely and reach the final steady state at the end of each time step, the slip rate parameter η_j can be simply specified according to Eq. (3) as:

$$\eta_j = \frac{a\pi\left(1-v_{j-1}\right)}{2G_{j-1}} \tag{S6}$$

which means that η at the jth time step is the function of the current effective elastic properties, qualitatively incorporating the effect of slip history to some extent although the frictional coefficient is kept constant.

Non-Interaction Approximation (NIA)

In addition, the Non-Interaction Approximation (NIA) is adopted at the end of the jth time step to calculate the eventual global strain by summing the contribution of all fractures slips. NIA originally assumes that any new fracture is surrounded by an undamaged elastic medium. Here we hypothesize that, within the jth time step, all critical fractures slip in an unchanged, homogeneous effective medium, which are the average properties updated at the end of the (j-1)th time step.

An example of iterative process

At the beginning of each time step, the elastic matrix strain $\boldsymbol{\varepsilon}^{\mathrm{m}}$ is first estimated according to Hooke's law under the plane strain condition:

$$\boldsymbol{\varepsilon}^m = \begin{bmatrix}\varepsilon_1^m\\ \varepsilon_3^m\end{bmatrix} = \frac{1-v}{2G}\begin{bmatrix}1 & -v/(1-v)\\ -v/(1-v) & 1\end{bmatrix}\begin{bmatrix}\sigma_1\\ \sigma_3\end{bmatrix} \tag{S7}$$

The relative displacement increments of each critical fracture within the time step are obtained based on Eq. (S5), Eq. (S6), and NIA, which are related to the global strain increments by Eq. (4) and further summed up to quantify the eventual additional strain tensor $\Delta\boldsymbol{\varepsilon}_{\mathrm{total},j}$:

$$\Delta\boldsymbol{\varepsilon}_{\mathrm{total}} = \begin{bmatrix}\Delta\varepsilon_1\\ \Delta\varepsilon_3\end{bmatrix} \tag{S8}$$

Taking compression as positive, $\Delta\varepsilon_3$ is always negative due to the fracture-induced dilation in the direction of the minor principal stress (σ_3). In the context of normal faulting stress regime, in which horizontal strain $\varepsilon_h = \varepsilon_3$ at boundary is maintained constant, the hortizontal strain of the elastic matrix ε_3^m needs to increase to accommodate $\Delta\varepsilon_3$, which is self-regulated by σ_3 increase.

Treating the model as an effective medium and invoking Hooke's law, we have the strain response at the *j*th time step as:

$$\varepsilon_{3,j} = \frac{1-v_{j-1}}{2G_{j-1}}\left(\frac{-v_{j-1}}{1-v_{j-1}}\sigma_{1,j-1} + \left(\sigma_{3,j-1} - \Delta\sigma_{3,j}\right)\right) + \Delta\varepsilon_{3,j} = \varepsilon_{3,0} \quad \text{(S9)}$$

which further gives:

$$\Delta\sigma_{3,j} = \frac{2G_{j-1}}{1-v_{j-1}}\Delta\varepsilon_{3,j} \quad \text{(S10)}$$

and

$$\sigma_{3,j} = \sigma_{3,j-1} - \Delta\sigma_{3,j} = \sigma_{3,j-1} - \frac{2G_{j-1}}{1-v_{j-1}}\Delta\varepsilon_{3,j} \quad \text{(S11)}$$

It implies a monotonic increase of σ_3 after each time step given a dilational $\Delta\varepsilon_{3,j}$. Accordingly, the updated strain $\varepsilon_{1,j}$ can be calculated by:

$$\varepsilon_{1,j} = \varepsilon_{1,j-1} + \frac{v_{j-1}}{2G_{j-1}}\Delta\sigma_{3,j} + \Delta\varepsilon_{1,j} \quad \text{(S12)}$$

where the second right-hand term reflects the Poisson effect induced by the increase of σ_3 and the third term is the slip-contributed strain increase. It should be noted that, the vertical stress is always constant in the normal faulting regime, i.e., $\sigma_v = \sigma_{1,0} = \sigma_{1,1} = \cdots = \sigma_{11,j-1} = \sigma_{11,j}$. With the updated global stress and strain at the boundary, effective elastic parameters (G_{j-1} and v_{j-1}) are updated by solving equations in Eq. (S7) at the end of the *j*th time step, acting as the input of the (*j*+1)th time step.

In addition to Figure 3**b**, more detailed information about the iterative process for frictional coefficient distribution $N(0.6, 0.05^2)$ can be found in Figure S2. The temporal variations of the slip rate parameter, slip rate, and shear stress difference of the most critical fracture show that the drastic rate of change in the first 1,000 time steps. The number of critical fractures within each time step further shows that it decreases rapidly from initially about 4,300 to 3 at around the 900th time step, explaining the slow growth of mechanical parameters during the subsequent tens of thousands of time steps as shown in Figure 3**b**. We also present the stochastic cases with frictional coefficient distribution (1) normal distribution $N(0.8, 0.06^2)$ and (2) Weibull distribution (scale parameter λ = 0.8 and shape parameter k = 10) in Figure S3 and Figure S4, respectively, where the first two iterations and the complete stress evolution process are included. As with the case specified in Figure 2, it confirms that the stochastic treatment of frictional coefficient is able to enable the model with local stress heterogeneity.

Text S3. Stress evolution for the deterministic case

For comparison, uniform frictional coefficient is assigned to all fractures while the model configuration remains the same. In Figure S5**a-d**, the first two iterations suggest a deterministic stress evolution process for the deterministic case. In other words, the equivalent frictional strength of the model is doubtlessly 0.6. At the beginning of each time step, all fractures lying above the frictional failure envelope are critical, which is not the case in the stochastic systems as shown in Figure 2 (or Figure S3 and Figure S4). In addition, shear stresses of all critical fractures will drop onto the single frictional failure line, i.e., frictional resistance. Due to the absence of heterogeneity, the deterministic system takes only 98 time steps to reach the final frictional equilibrium, as shown in Figure S5**e**. This gives a quantitative interpretation of the classic notion of frictional equilibrium and also confirms that the very control of the most critical fracture on the global stress state.

Text S4. Monte Carlo simulation, system uncertain analysis

Whether a fracture is critical or not depends on its frictional coefficient and orientation with respect to the global stress field. As both parameters are randomly generated in each experimentation, it is imperative to examine the uncertainty associated with this stochastic model. To this end, we run 10,000 Monte Carlo simulations to repeat the iterative process. Primarily, we quantify the probability of the frictional coefficient and orientation of the most critical fracture, to see if it stays invariant to support our conclusions.

For each simulation, the frictional coefficient and orientation of the fractures are randomly generated according to the respective distribution. We apply the same initial stress difference (σ_h = $\sigma_{1,0}$ = 100 MPa > σ_v = $\sigma_{3,0}$ = 20 MPa) in the normal faulting scenario (shown in Figure 4). It is then able to identify the most critical fracture by determining the largest shear stress difference $\Delta\tau$. Figure S6 shows the distributions of the frictional coefficient and orientation of the most critical fracture in different cases. In Figure S6**a-c**, we confirm that the frictional coefficient of the most critical fracture falls at the lower end of its distribution. With regard to the orientation, the most critical fracture orients approximately at an angle of 60° or 120° to the global horizontal axis, as shown in Figure S6**d-f**. In addition, the uncertainty of both parameters increases as the system becomes more heterogeneous. It should be noted that the final Mohr circle is not necessary tangent to the frictional failure envelope in the stochastic case. As an end-member, the frictional coefficient and orientation of the most critical fracture in the deterministic case are also deterministic (Figure S5). Since frictional coefficient distribution is used as a proxy of system heterogeneity, it is concluded that the global response also has remarkable uncertainty which depends largely on the intrinsic heterogeneity. In the context of normal faulting stress regime, such uncertainty can be represented by distributed frictional failure envelope, or more quantitatively, by the probability density function of effective minor principal stress σ_3 determined at the end of each simulation, as shown in Figure 4.

Text S5. Stress evolution in the context of reverse faulting stress regime

For each distribution, we also experimented the model in the context of reverse faulting regime. To facilitate comparison, we set the same starting stress difference ($\sigma_h = \sigma_{1,0}$ = 100 MPa > $\sigma_v = \sigma_{3,0}$ = 20 MPa). We maintain the boundary condition of constant vertical stress and constant lateral strain. Based on the expressions in the normal faulting case, we can obtain similar derivations simply by switching the numeric subscripts '1' and '3' of each term in Eq. (S11), which gives:

$$\sigma_{1,j} = \sigma_{1,j-1} - \Delta\sigma_{1,j} = \sigma_{1,j-1} - \frac{2G_{j-1}}{1-v_{j-1}}\Delta\varepsilon_{1,j} \tag{S13}$$

Note that, $\Delta\varepsilon_{1,j}$ is positive due to compression in this scenario. Therefore, σ_1 will decrease and the updated strain $\varepsilon_{3,j}$ can be calculated by:

$$\varepsilon_{3,j} = \varepsilon_{3,j-1} + \frac{v_{j-1}}{2G_{j-1}}\Delta\sigma_{1,j} + \Delta\varepsilon_{3,j} \tag{S14}$$

Figure S7-S9 show the first two iterations and the whole stress evolution process for frictional coefficient distribution (1) normal distribution $N(0.8, 0.06^2)$, (2) normal distribution $N(0.6, 0.05^2)$, and (3) Weibull distribution (λ = 0.8, k = 10), respectively. As expected, lateral stress $\sigma_{1,j}$ decreases to allow for the reduction of stress difference due to frictional slip. The final stress difference is smaller than that of the normal faulting scenario, for any distribution, and it takes much more time steps reach the final frictional equilibrium. We further note that, for each distribution, the frictional equilibrium in both stress regimes is bounded by the same equivalent frictional strength. This reveals that the equivalent frictional strength of the model is independent of the applied boundary conditions, but characteristic of the stochastic nature of the fractures therein. In addition, the deterministic case in reverse faulting regime is shown in Figure S10. As with the stochastic cases, it takes much more time steps to reach the final frictional equilibrium than the normal faulting scenario.

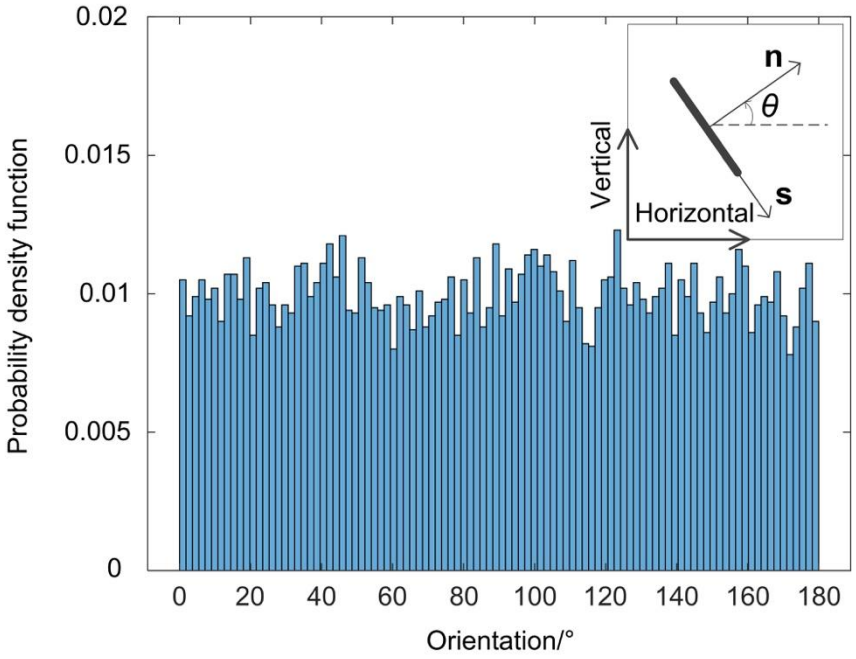

Figure S1. Uniform distribution of fracture orientation, which is defined schematically in the inset.

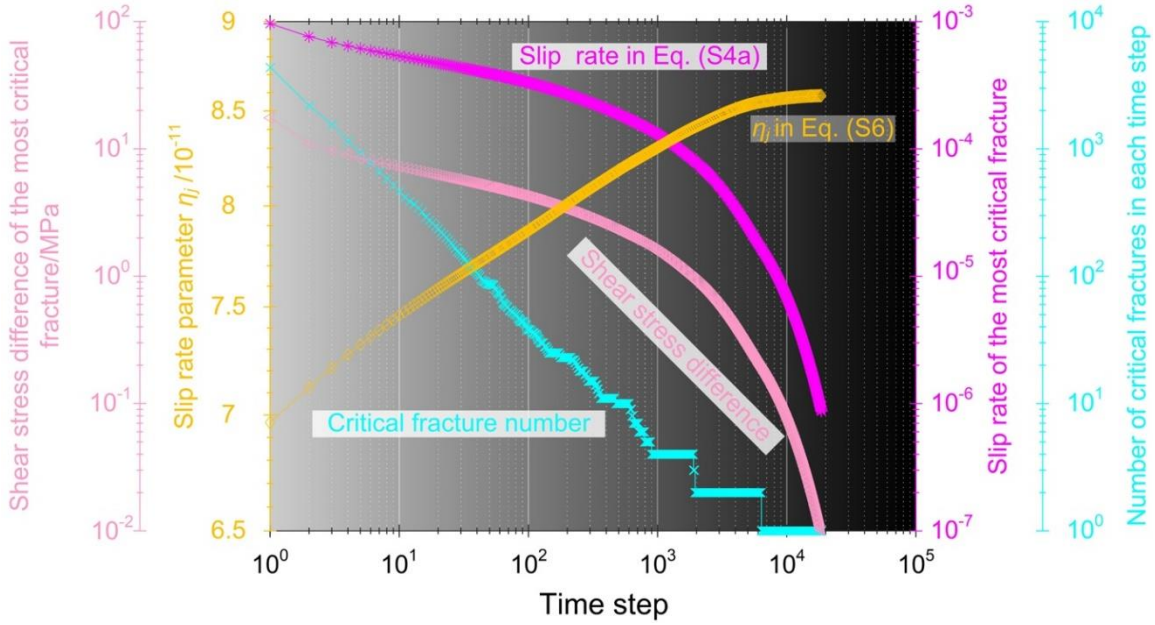

Figure S2. Evolution of slip rate parameter, slip rate, and shear stress difference of the most critical fracture, and critical fracture number in each time step in the stochastic case specified in Figure 2.

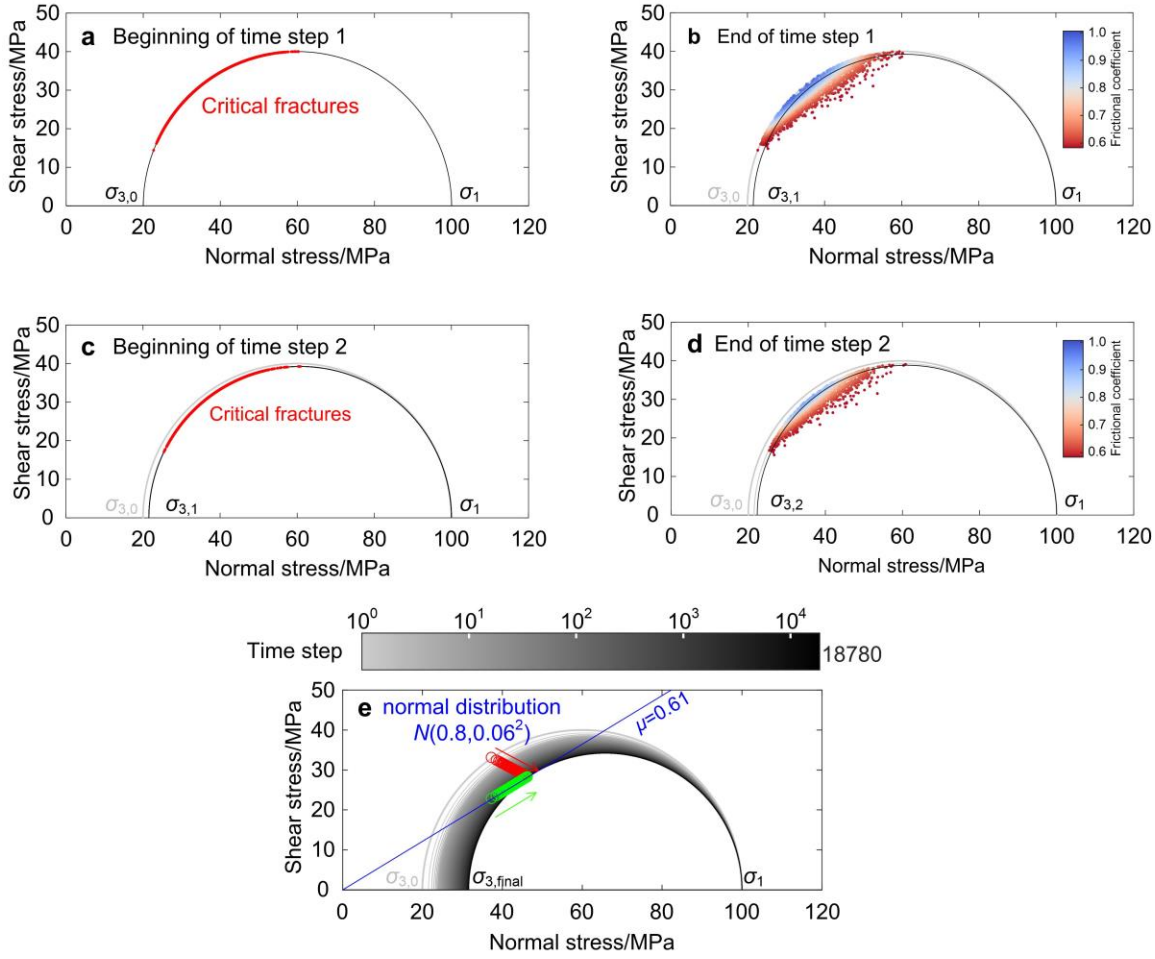

Figure S3. Stochastic case with normally distributed frictional coefficient $N(0.8, 0.06^2)$ in normal faulting stress regime: **a-d** Identification of critical fractures and stress evolution in the first two iterations. For each time step, critical fractures are identified at its beginning, which are marked as red dot on the Mohr diagram. After frictional slip, stress state of each critical fracture is colored according to its frictional coefficient. **e** Complete process of stress evolution. Red circle represents the resolved stress state surrounding the most critical fracture at each time step, while green circle is its frictional resistance. As a reference, the frictional coefficient of the most critical fracture is plotted as a solid blue line. Gray colormap is also shown with color scaled to time step. The total number of time steps is 18,780.

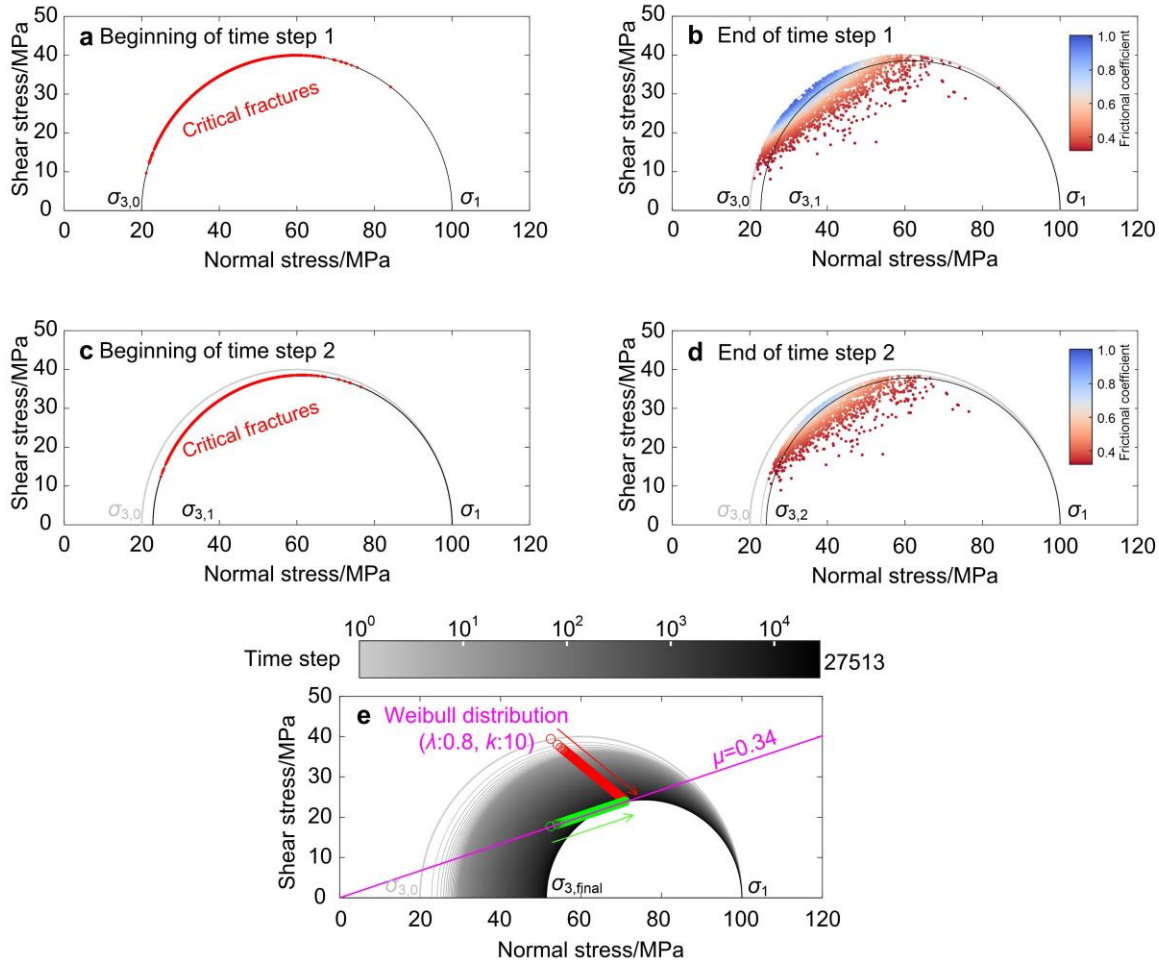

Figure S4. Stochastic system with frictional coefficient following Weibull distribution (λ = 0.8, k = 10) in normal faulting stress regime: **a-d** Identification of critical fractures and stress evolution in the first two iterations. For each time step, critical fractures are identified at its beginning, which are marked as red dot on the Mohr diagram. After frictional slip, stress state of each critical fracture is colored according to its frictional coefficient. **e** Complete process of stress evolution. Red circle represents the resolved stress state surrounding the most critical fracture at each time step, while green circle is its frictional resistance. As a reference, the frictional coefficient of the most critical fracture is plotted as a solid magenta line. Gray colormap is also shown with color scaled to time step. The total number of time steps is 27,513.

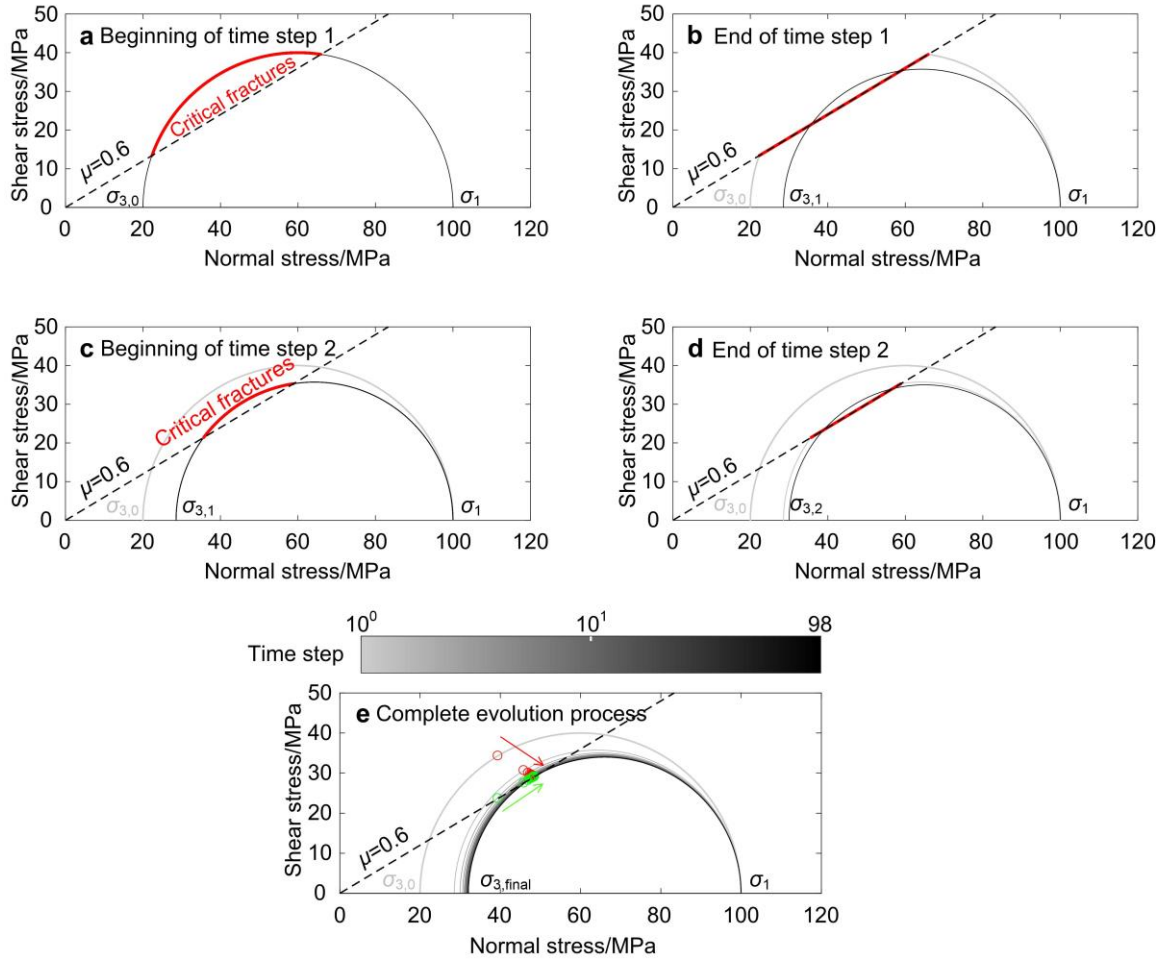

Figure S5. Deterministic case with equal frictional coefficient (0.6) in normal faulting stress regime: **a-d** Identification of critical fractures and stress evolution in the first two iterations. For each time step, critical fractures are identified at its beginning, which are marked as red dot on the Mohr diagram. After frictional slip, all critical fractures are represented as red dots on the frictional failure line (black dashed line). **e** Complete process of stress evolution. Red circle represents the resolved stress state surrounding the most critical fracture at each time step, while green circle is its frictional resistance. Gray colormap is shown with color scaled to time step. The total number of time steps is 98.

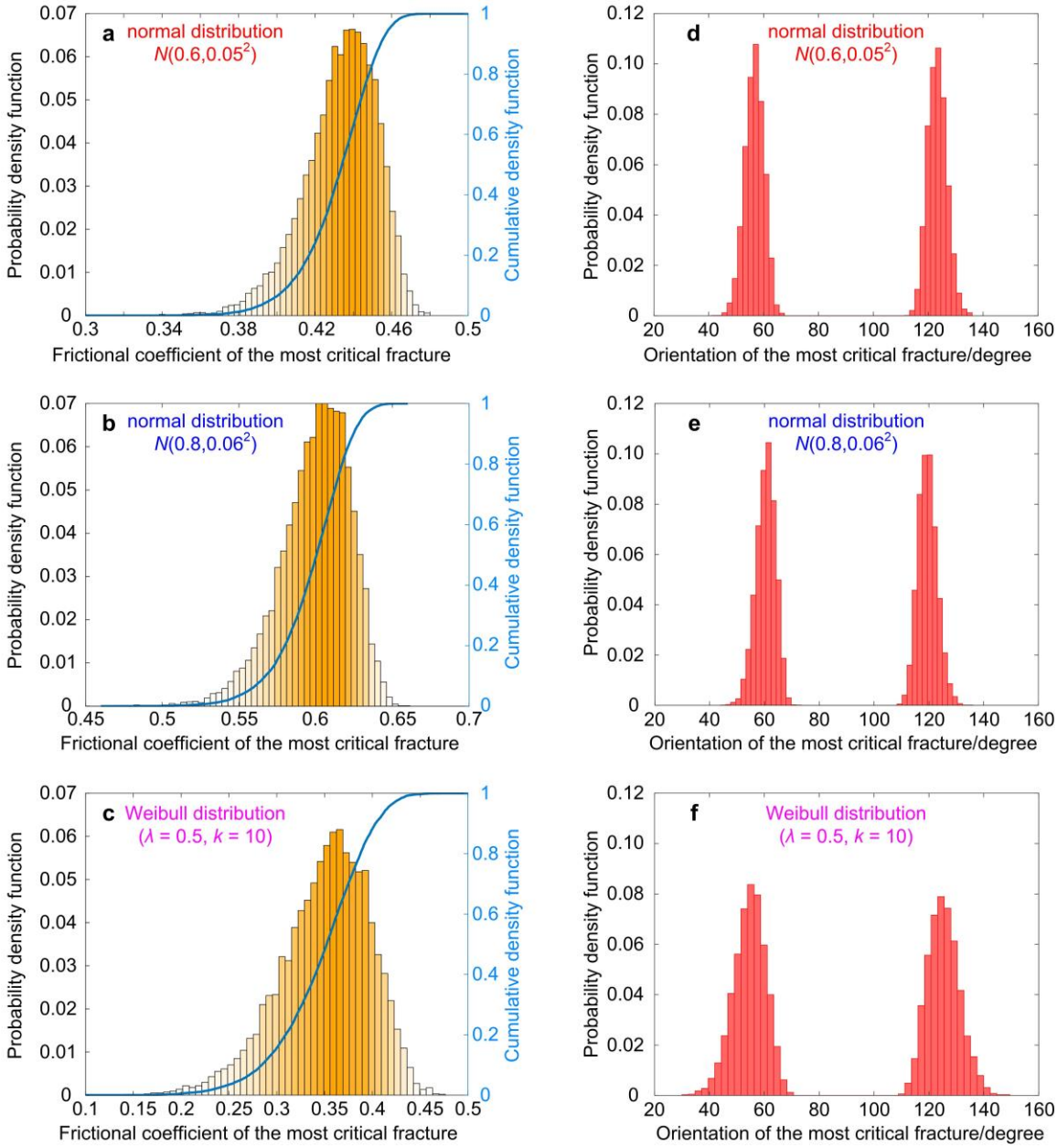

Figure S6. Probability density function of the (**a-c**) frictional coefficient and (**d-f**) orientation of the most critical fracture based on 10,000 calculations for each frictional coefficient distribution, using Monte Carlo method. The color gradient of each bin in (**a-c**) is scaled to its probability.

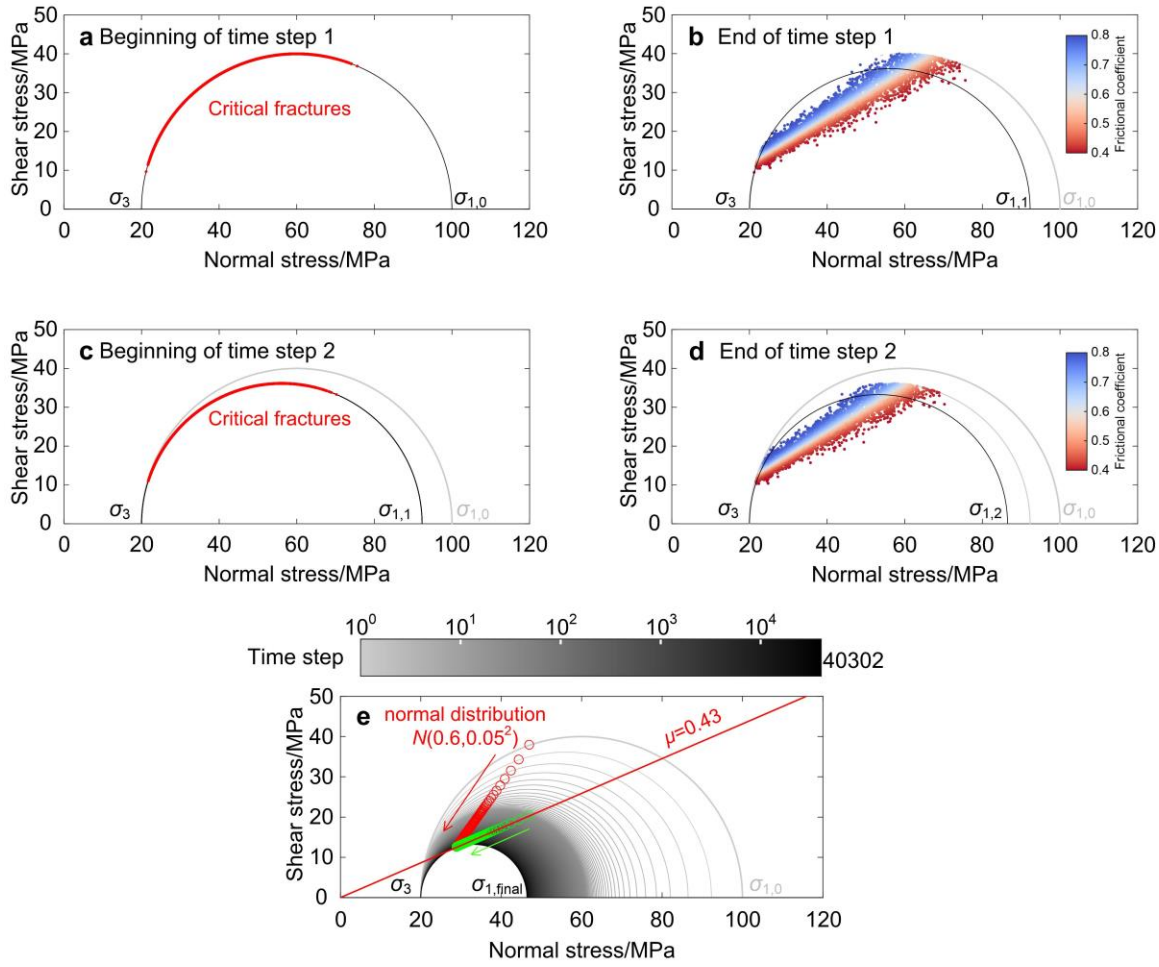

Figure S7. Stochastic system with normally distributed frictional coefficient $N(0.6,\ 0.05^2)$ in reverse faulting stress regime: **a-d** Identification of critical fractures and stress evolution in the first two iterations. For each time step, critical fractures are identified at its beginning, which are marked as red dot on the Mohr diagram. After frictional slip, stress state of each critical fracture is colored according to its frictional coefficient. **e** Complete process of stress evolution. Red circle represents the resolved stress state surrounding the most critical fracture at each time step, while green circle is its frictional resistance. As a reference, the frictional coefficient of the most critical fracture is plotted as a solid red line. Gray colormap is also shown with color scaled to time step. The total number of time steps is 40,302.

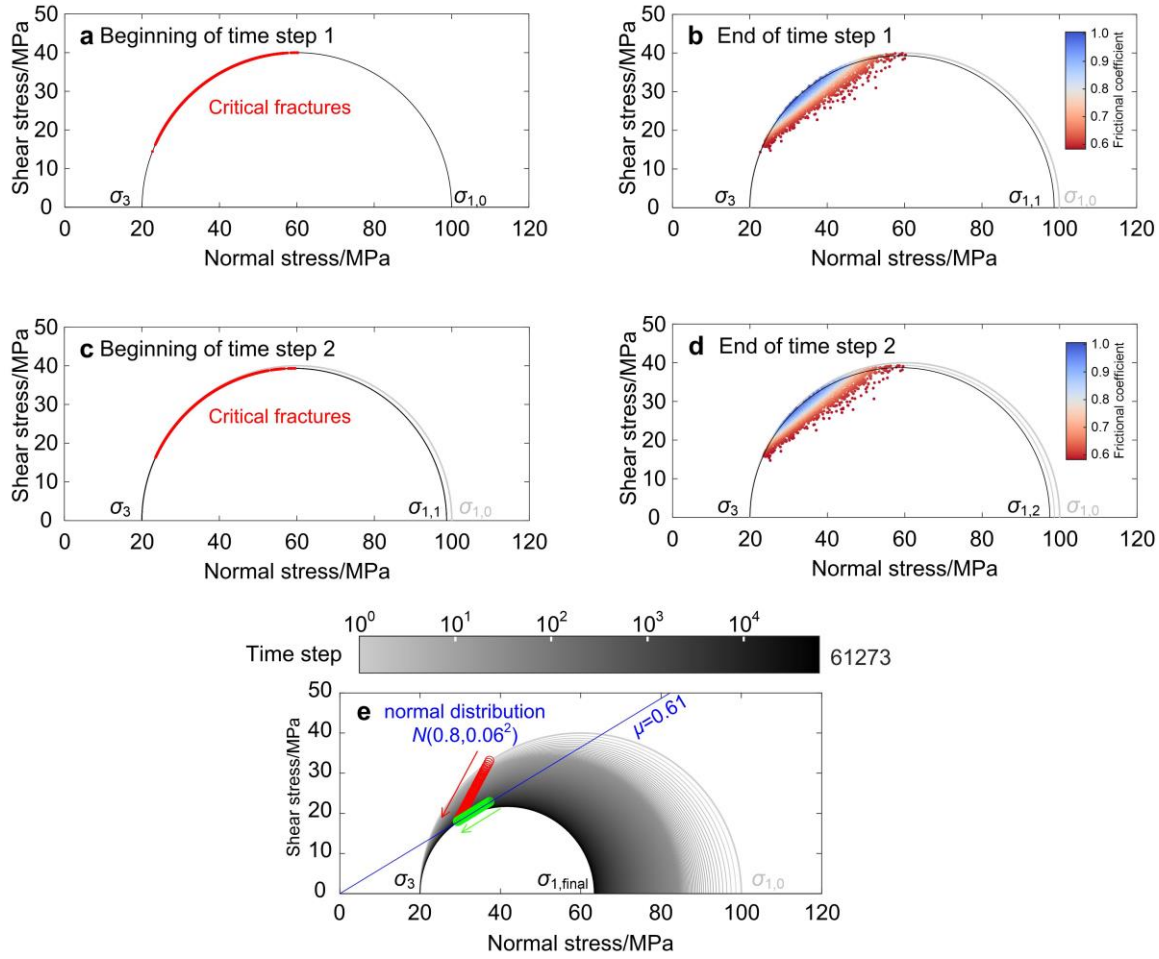

Figure S8. Stochastic system with normally distributed frictional coefficient $N(0.8, 0.06^2)$ in reverse faulting stress regime: **a-d** Identification of critical fractures and stress evolution in the first two iterations. For each time step, critical fractures are identified at its beginning, which are marked as red dot on the Mohr diagram. After frictional slip, stress state of each critical fracture is colored according to its frictional coefficient. **e** Complete process of stress evolution. Red circle represents the resolved stress state surrounding the most critical fracture at each time step, while green circle is its frictional resistance. As a reference, the frictional coefficient of the most critical fracture is plotted as a solid blue line. Gray colormap is also shown with color scaled to time step. The total number of time steps is 61,273.

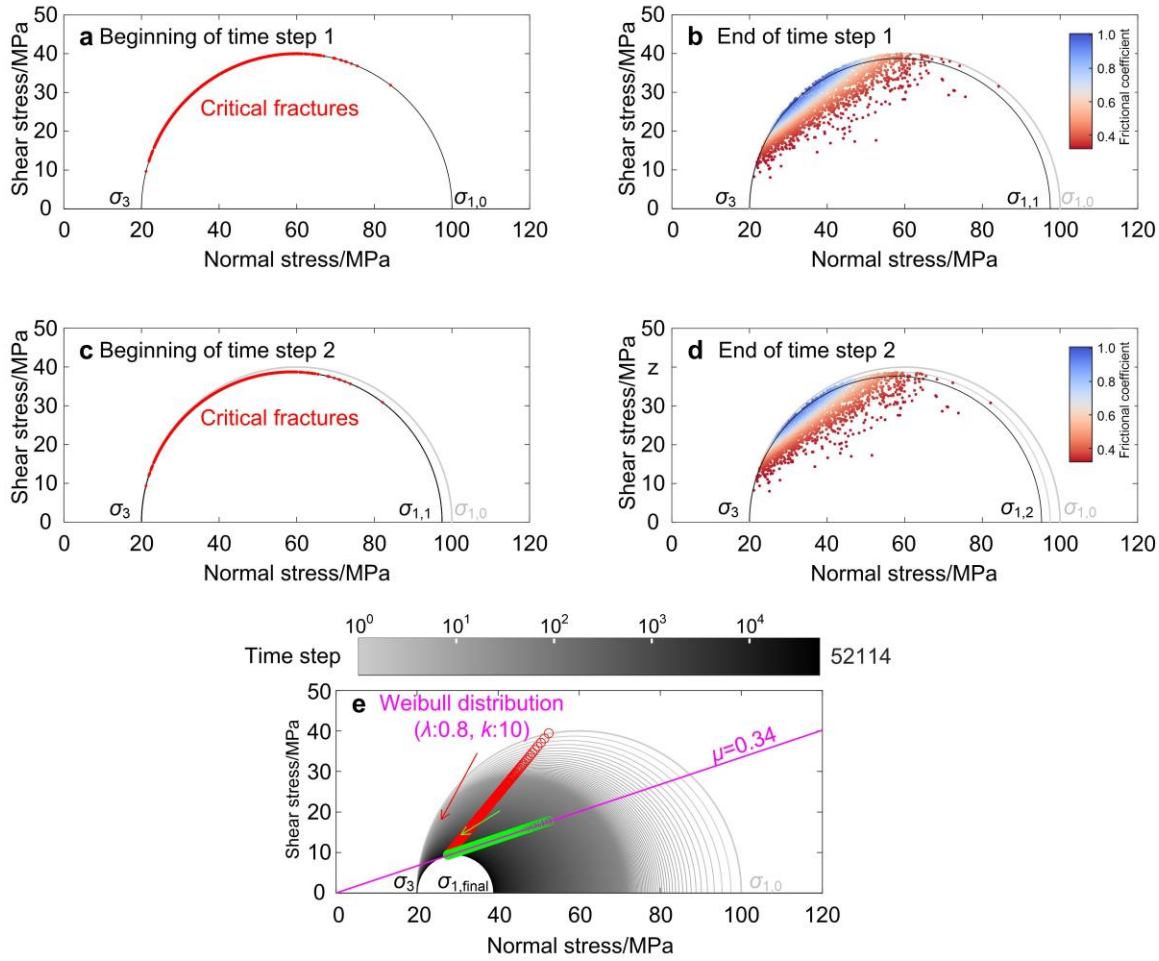

Figure S9. Stochastic system with frictional coefficient following Weibull distribution (λ = 0.8, k = 10) in reverse faulting stress regime: **a-d** Identification of critical fractures and stress evolution in the first two iterations. For each time step, critical fractures are identified at its beginning, which are marked as red dot on the Mohr diagram. After frictional slip, stress state of each critical fracture is colored according to its frictional coefficient. **e** Complete process of stress evolution. Red circle represents the resolved stress state surrounding the most critical fracture at each time step, while green circle is its frictional resistance. As a reference, the frictional coefficient of the most critical fracture is plotted as a solid red line. Gray colormap is also shown with color scaled to time step. The total number of time steps is 52,114.

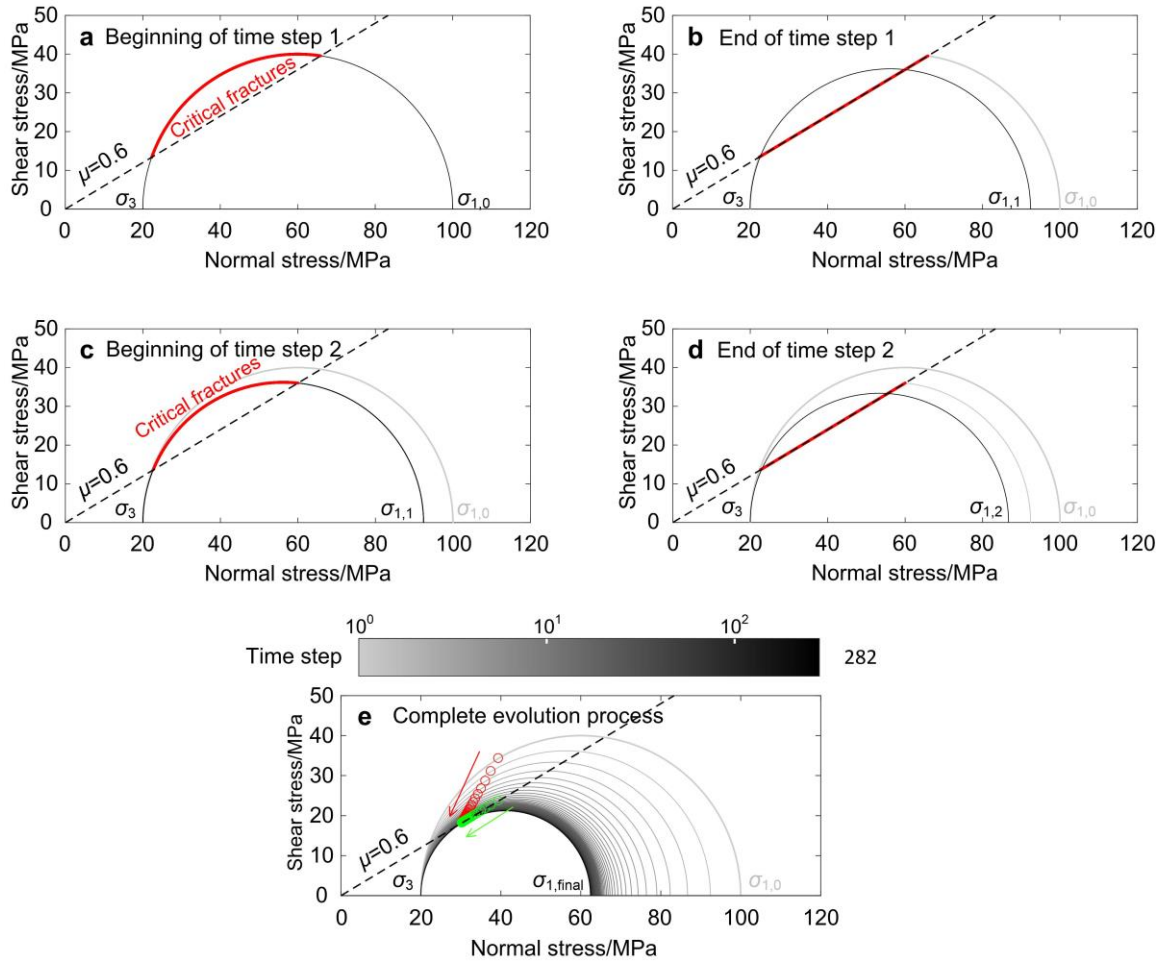

Figure S10. Deterministic case with equal frictional coefficient (0.6) in reverse faulting stress regime: **a**-**d** Identification of critical fractures and stress evolution in the first two iterations. For each time step, critical fractures are identified at its beginning, which are marked as red dot on the Mohr diagram. After frictional slip, all critical fractures are represented as red dots on the frictional failure line (black dashed line). **e** Complete process of stress evolution. Red circle represents the resolved stress state surrounding the most critical fracture at each time step, while green circle is its frictional resistance. Gray colormap is shown with color scaled to time step. The total number of time steps is 282.